



How Well Do Multisatellite Products Capture the Space–Time Dynamics of Precipitation? Part II: Building an Error Model through Spectral System Identification

CLEMENT GUILLOTEAU,^a EFI FOUFOULA-GEORGIU,^{a,b} PIERRE KIRSTETTER,^{c,d} JACKSON TAN,^{e,f}
AND GEORGE J. HUFFMAN^f

^a *Department of Civil and Environmental Engineering, University of California, Irvine, Irvine, California*

^b *Department of Earth System Science, University of California, Irvine, Irvine, California*

^c *Hydrometeorology and Remote Sensing Laboratory, University of Oklahoma, Norman, Oklahoma*

^d *NOAA Severe Storms Laboratory, Norman, Oklahoma*

^e *NASA Goddard Space Flight Center, Greenbelt, Maryland*

^f *University of Maryland, Baltimore County, Catonsville, Maryland*

(Manuscript received 8 March 2022, in final form 7 June 2022)

ABSTRACT: Satellite precipitation products, as all quantitative estimates, come with some inherent degree of uncertainty. To associate a quantitative value of the uncertainty to each individual estimate, error modeling is necessary. Most of the error models proposed so far compute the uncertainty as a function of precipitation intensity only, and only at one specific spatio-temporal scale. We propose a spectral error model that accounts for the neighboring space–time dynamics of precipitation into the uncertainty quantification. Systematic distortions of the precipitation signal and random errors are characterized distinctively in every frequency–wavenumber band in the Fourier domain, to accurately characterize error across scales. The systematic distortions are represented as a deterministic space–time linear filtering term. The random errors are represented as a nonstationary additive noise. The spectral error model is applied to the IMERG multisatellite precipitation product, and its parameters are estimated empirically through a system identification approach using the GV-MRMS gauge–radar measurements as reference (“truth”) over the eastern United States. The filtering term is found to be essentially low-pass (attenuating the fine-scale variability). While traditional error models attribute most of the error variance to random errors, it is found here that the systematic filtering term explains 48% of the error variance at the native resolution of IMERG. This fact confirms that, at high resolution, filtering effects in satellite precipitation products cannot be ignored, and that the error cannot be represented as a purely random additive or multiplicative term. An important consequence is that precipitation estimates derived from different sources shall not be expected to automatically have statistically independent errors.

SIGNIFICANCE STATEMENT: Satellite precipitation products are nowadays widely used for climate and environmental research, water management, risk analysis, and decision support at the local, regional, and global scales. For all these applications, knowledge about the accuracy of the products is critical for their usability. However, products are not systematically provided with a quantitative measure of the uncertainty associated with each individual estimate. Various parametric error models have been proposed for uncertainty quantification, mostly assuming that the uncertainty is only a function of the precipitation intensity at the pixel and time of interest. By projecting satellite precipitation fields and their retrieval errors into the Fourier frequency–wavenumber domain, we show that we can explicitly take into account the neighboring space–time multiscale dynamics of precipitation and compute a scale-dependent uncertainty.

KEYWORDS: Precipitation; Remote sensing; Satellite observations; Error analysis; Fourier analysis; Spectral analysis/models/distribution; Model errors

Denotes content that is immediately available upon publication as open access.

Supplemental information related to this paper is available at the Journals Online website: <https://doi.org/10.1175/JHM-D-22-0041.s1>.

Corresponding author: Clement Guilloteau, cguillot@uci.edu

1. Introduction

A large body of literature focuses in evaluating the accuracy of satellite quantitative precipitation estimation (QPE) products [see, e.g., Derin et al. (2016), Petersen et al. (2020), chapters 1 and 3 in Roca et al. (2021), and Pradhan et al. (2022) for a selective overview]. While this substantial evaluation work provides useful insights on the local, regional, and global accuracy of satellite QPEs, it has not converged to a unified framework for diagnosing the nature of the errors and for quantifying and

DOI: 10.1175/JHM-D-22-0041.1

© 2022 American Meteorological Society. For information regarding reuse of this content and general copyright information, consult the [AMS Copyright Policy](#) (www.ametsoc.org/PUBSReuseLicenses).

predicting the retrieval accuracy at any time and location. Still today, only few (Chambon et al. 2013b) of the existing operational satellite QPEs are provided with a quantification of the uncertainty associated with each individual estimate. Constructing a statistical error model applicable to satellite QPE products is the first necessary step toward achieving these objectives.

In Guilloteau et al. (2021) a three-dimensional Fourier wave-number–frequency analysis was performed to evaluate the ability of five multisatellite QPEs to reproduce the space–time dynamics of precipitation. Such an evaluation examines the dynamical variability of the precipitation field over space and time, instead of the conventional point-by-point or pixel-by-pixel comparison of values; it provides information about the multiscale space–time structure of the error and can give insights about its nature. Indeed, the distortions that affect QPEs are expected to be of various nature, among which are not only systematic biases (e.g., from imperfect instrumental or algorithmic calibration) and random noise (instrumental noise or environmental noise), but also geometric distortions (due to the observation geometry and instruments’ limited resolution), mislocation and mistiming of the precipitation features, and linear and nonlinear filtering effects. The spectral characteristics of the satellite-derived precipitation in Guilloteau et al. (2021) were compared to those of the GV-MRMS gauge–radar fields over the southeastern United States. It was found that all satellite QPEs are too spatially and temporally “smooth,” with a deficit of spectral power at spatial wavelengths shorter than 200 km and temporal periods shorter than 3 h, i.e., excessive short-range correlation. This important characteristic of the retrieved precipitation fields is not quantified by most of the error models which have been applied to QPEs. Indeed, classical error models generally decompose the error into a random term, which can be an additive or multiplicative noise, and systematic term, which is generally a function of the precipitation intensity only (e.g., AghaKouchak et al. 2012; Kirstetter et al. 2013; Tian et al. 2013; Maggioni et al. 2014, 2016; Wright et al. 2017; Tang 2020; Tang et al. 2021). Eventually, all the information provided by these types of error model can be reduced to the joint probability density of the retrieved precipitation against the true precipitation, at a specified space–time resolution, therefore ignoring the spatial and temporal structure and multiscale properties of the error field. We propose here an alternative methodology that consists of decomposing the error into a systematic multiplicative term which is a function of temporal frequency and spatial wavenumber, i.e., a three-dimensional linear filtering operator, plus a random noise term. By accounting for the dependence of both the systematic and random components of the error on spatial and temporal scales through the wavenumber–frequency decomposition, we can arguably provide a more comprehensive representation of the error. This spectral error model is developed herein and applied to the IMERG precipitation product with the GV-MRMS gauge–radar data serving as a reference for the estimation of the model parameters.

The conceptual spectral error model is introduced in section 2. Section 3 presents the application of the spectral error model to the IMERG multisatellite QPE using the GV-MRMS data as a reference for calibration. Section 4 discusses the questions of nonstationarity and heteroscedasticity and the dependence of the

model parameters on geographical locations, climate type and season, as well as the local dependence between the power spectra of the noise and of precipitation itself. The implications of such an error model to QPE evaluation and multisource merging are discussed in section 5, before the concluding remarks.

2. A spectral error model based on linear system theory

The results of the characterization of the satellite QPE errors in the frequency–wavenumber domain presented in Guilloteau et al. (2021) demonstrated that, in some frequency and wavenumber bands, the error is not linearly independent from the true precipitation signal and therefore, cannot be represented as a pure random process (as for example an additive or multiplicative noise with zero expected value). Indeed, if the error was random and linearly independent from the true precipitation at all frequencies and wavenumbers, the power spectral density (PSD) of the retrieved precipitation would be equal to the sum of the PSD of the true precipitation and the PSD of the error. However, Guilloteau et al. (2021) found that satellite QPEs have a lower PSD than the gauge–radar precipitation (which is considered as an accurate proxy of the truth) over a wide range of wavenumbers and frequencies (Fig. 1, bottom-left panel), revealing that linear dependences exist between the true precipitation and the retrieval error in the corresponding frequency and wavenumber bands. This dependence can be represented as a frequency-and-wavenumber-dependent systematic multiplicative bias, i.e., a linear invariant filtering operation. In addition to this deterministic linear filtering term, some nonlinearities or randomness also exist in the spectral relationships between the true and retrieved precipitation, as indicated by the fact that their spectral coherence is not equal to one at all frequencies and wavenumbers (Fig. 1, bottom-right panel; more details in Guilloteau et al. 2021).

In this study, these spectral characteristics of the retrieval error are accounted for by representing the retrieval process as a linear system, where the true precipitation is one input and the retrieved precipitation is the output. This type of linear system representation is classically used in the fields of signal processing and electrical and mechanical engineering (Swisher 1976; Chen et al. 2004; Chen 2012); it also has been applied extensively in hydrology to represent the hydrological response of a basin to precipitation (Dooge 1973; Bras and Rodriguez-Iturbe 1993; Jukić and Denić-Jukić 2004; Jiménez-Martínez et al. 2013; Schuite et al. 2019), and, as in the present paper, to represent and model an observation system (Andricevic and Foufoula-Georgiou 1991). Our system representation of the retrieval process consists of the addition of a noise to the precipitation signal, followed by a linear invariant filtering operation in both space and time. The relation between the retrieved (estimated) precipitation R_e and the true precipitation R is therefore modeled as

$$R_e(x, y, t) = H(x, y, t) * [R(x, y, t) + N(x, y, t)], \quad (1)$$

where $\{x, y, t\}$ are the space–time coordinates, $*$ is the convolution operator, and $H(x, y, t)$ is a deterministic space–time convolution kernel (as for example a Gaussian smoothing kernel, or on

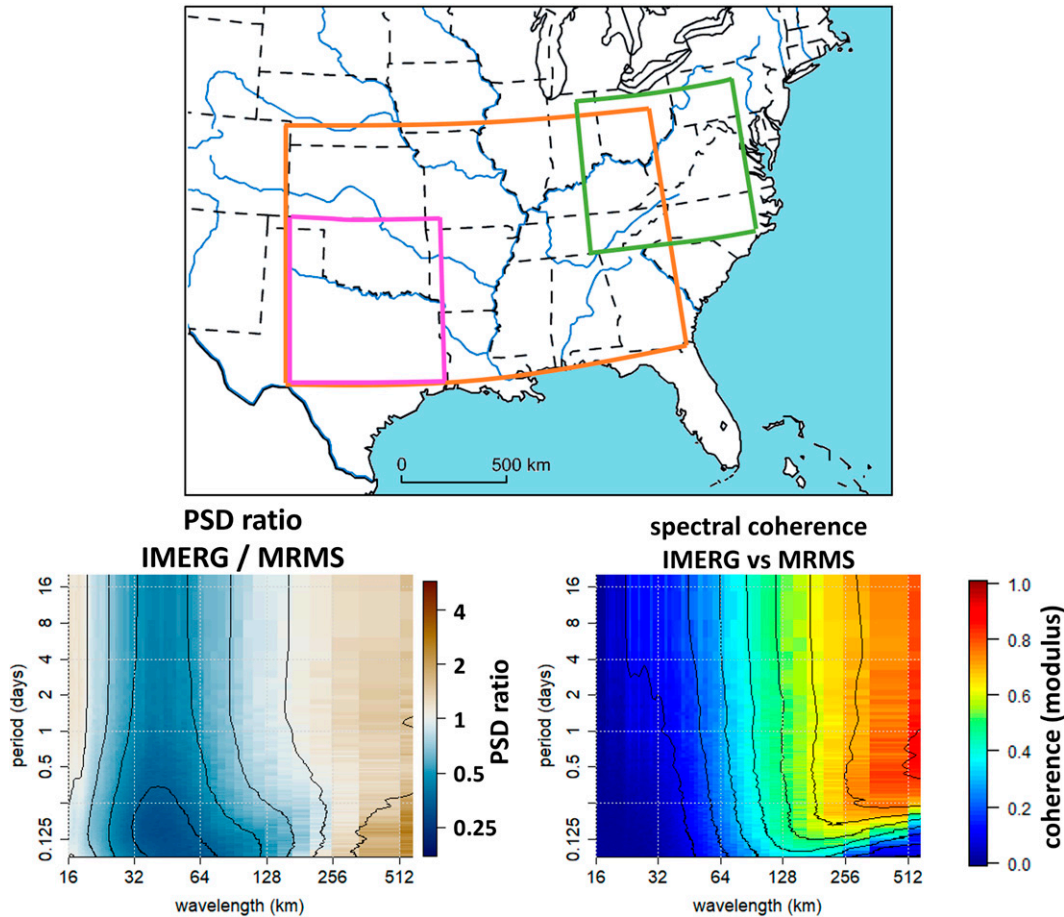


FIG. 1. (top) Map of the study area. The orange box corresponds to the southeastern United States region (30°–41°N, 81°–102°W) used for the Guilloteau et al. (2021) study and in the present study. The purple and green boxes are, respectively, the Oklahoma and northeastern Texas (30°–37°N, 95°–102°W) and the Appalachian Mountains (35°–42°N, 78°–85°W) subregions used here to evaluate the variability of the spectral error model parameters across different climates (see Fig. 14). (bottom) Results of the Guilloteau et al. (2021) study for the IMERG product: (left) ratio of the PSD of IMERG over the PSD of GV-MRMS and (right) spectral coherence between IMERG and GV-MRMS as functions of the Fourier spatial wavelength and temporal period.

the contrary a “sharpening” differential kernel). The noise N is defined as having a zero expected value and being linearly independent from the true precipitation signal R . Nonlinear dependences, which will be further discussed in the article, may, however, exist between N and R . The noise is expected to be spatially and temporally correlated, meaning that its PSD is expected to vary with frequency and wavenumber; it is therefore not assumed to be a white noise (with a “flat” PSD). In the Fourier domain, Eq. (1) becomes

$$\hat{R}_e(k_x, k_y, f) = \hat{H}(k_x, k_y, f) \times [\hat{R}(k_x, k_y, f) + \hat{N}(k_x, k_y, f)]. \tag{2}$$

The hat ($\hat{\cdot}$) operator represents the Fourier transform; k_x, k_y are the longitudinal and latitudinal wavenumbers; and f is the temporal frequency. The filtering operator, characterized by its transfer function $\hat{H}(k_x, k_y, f)$, represents the systematic

frequency-and-wavenumber-dependent distortions of the retrieved precipitation signal, as compared to the truth. As H may not be an even function of space and time, its Fourier transform \hat{H} is generally a complex function. An argument of $\hat{H}(k_x, k_y, f)$ different from zero indicates the existence of a systematic phase shift between the retrieved and the true precipitation. Figure 2 shows a block-diagram representation of this simple linear system.

Following a classical system identification approach (Keesman 2011), the identification of the spectral error model consists in determining the transfer function $\hat{H}(k_x, k_y, f)$ and the PSD of the noise $\Gamma_N(k_x, k_y, f)$. For the system to be identifiable we assume that N and R are linearly independent in the Fourier domain, i.e., their cross power spectral density (CPSD), $\Gamma_{N,R}(k_x, k_y, f)$ is null at all frequencies and wavenumbers. With such a model, the error $R_e - R$ can eventually be decomposed in two terms:

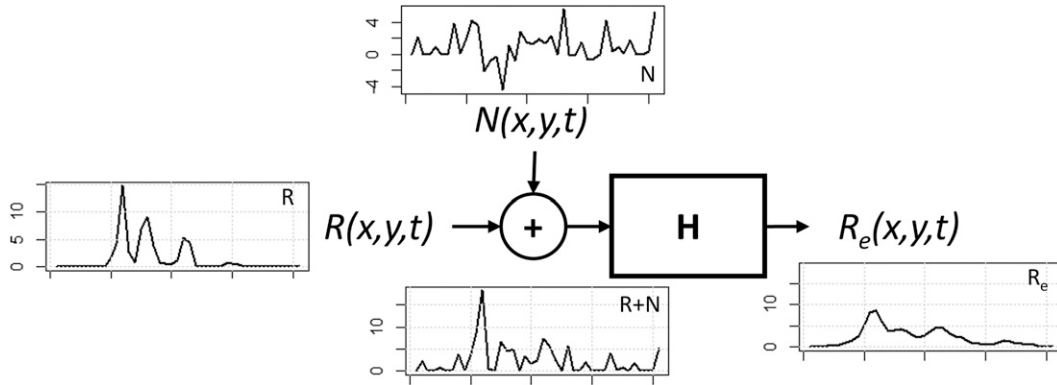


FIG. 2. Linear system block diagram representation of the idealized retrieval process used to construct the spectral error model. The retrieved precipitation R_e is described as the result of the space–time convolution of the true precipitation signal R plus the noise N with the deterministic kernel H . A convolution in the space–time domain corresponds to a multiplication in the Fourier domain, i.e., a linear filtering operation. Time series are generated synthetically to provide a simple 1D illustrative example, with a white noise and a Gaussian smoothing kernel.

$$R_e - R = (H * N) + [(H * R) - R]. \tag{3}$$

The first term represents the residual noise after the filtering operator and the second term represents the precipitation signal “lost” because of the filtering operator. Because these two terms are orthogonal, the sum of their respective variance equals the variance of the error:

$$\text{var}(R_e - R) = \text{var}(H * N) + \text{var}[(H * R) - R]. \tag{4}$$

We can therefore define the fraction τ of the error variance coming from the filtering effect as

$$\tau = \frac{\text{var}[(H * R) - R]}{\text{var}(R_e - R)}, \tag{5}$$

and conversely, the fraction of the error coming from the noise as

$$1 - \tau = \frac{\text{var}(H * N)}{\text{var}(R_e - R)}. \tag{6}$$

The parameters of the spectral error model may be estimated through a heuristic analysis of the retrieval process itself, assuming that each element of this process can be modeled mathematically. However, for a multisatellite precipitation product relying on a dozen of different instrumental measurements and multiple calibration and processing layers, this may be practically unfeasible. We chose here instead to follow a data-oriented benchmarking approach by comparing the multisatellite estimates to a trusted reference measurement considered as the “truth” as described in the next section. The errors and uncertainty of this reference estimate are deemed negligible compared to those of the satellite QPE.

3. The spectral error model applied to the IMERG product

a. Satellite and gauge–radar data

The data used in the present study are identical to the data used in [Guilleteau et al. \(2021\)](#). The GV-MRMS gauge–radar data ([Kirstetter et al. 2012](#); [Petersen et al. 2020](#)) are used as the “ground truth” for estimating the parameters of the spectral error models of the satellite QPEs. The eastern part of the United States ([Fig. 1](#), top) is targeted because the radar and gauge coverage are sufficiently good to provide a robust ground truth at the 10-km and 30-min resolution. The present study focuses on the IMERG V06 Final Run product (IMERG hereafter; [Huffman et al. 2019](#)), because IMERG was found to perform the best among the evaluated satellite products in [Guilleteau et al. \(2021\)](#). The “uncalibrated” IMERG precipitation estimates, which are used in this study, are satellite-only and do not include gauge adjustment (unlike the “calibrated” precipitation estimates, which are also provided in the IMERG Final Run product). The results for the other multisatellite QPEs, namely, the near-real-time “Early” version of IMERG, CMORPH (V1.0), GSMaP (V7), and PERSIANN-CCS are made available to the readers as online supplemental material. As in [Guilleteau et al. \(2021\)](#), data from the January 2018 to April 2020 period are used. The months of March 2018 and March 2019 were excluded for having too many measurements not meeting the quality requirements of the GV-MRMS quality control.

b. Estimation of the model parameters

When R_e and R are known, the identification of the model parameters is straightforward. The transfer function \hat{H} is computed as

$$\hat{H}(k_x, k_y, f) = \frac{\Gamma_{R_e R_e}(k_x, k_y, f)}{\Gamma_R(k_x, k_y, f)}, \tag{7}$$

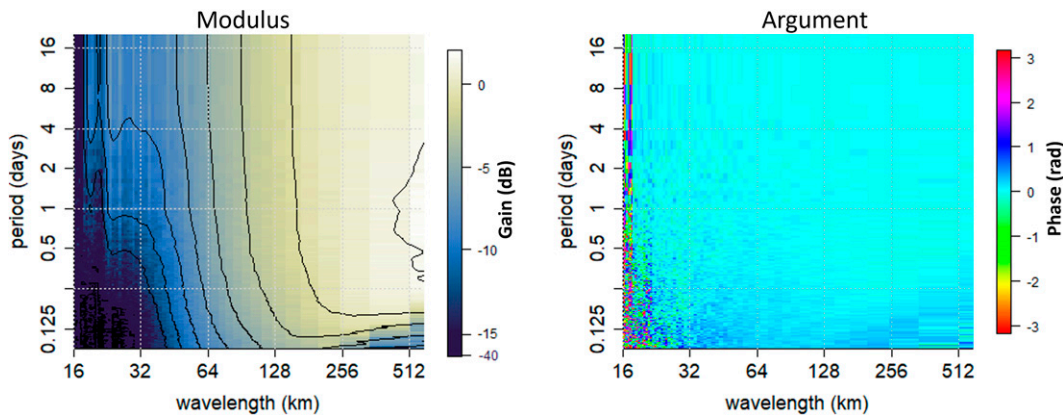


FIG. 3. Empirical transfer function $\hat{H}(k, f)$ of IMERG estimated against GV-MRMS from two years of data over the southeastern United States. Both the modulus (gain) and argument (phase) are shown as functions of the spatial wavelength $\lambda = 1/k$ and temporal period $p = 1/f$. Smoothed isocontours are added over the colormaps to improve visualization.

where Γ_R is the PSD of R , and Γ_{R,R_e} is the CPSD of R and R_e . We note that in practice, with finite amount of data, some regularization is always necessary in the estimation of Γ_R and Γ_{R,R_e} to avoid overfitting (see appendix). Once \hat{H} is identified, the PSD of the noise component is computed as

$$\Gamma_N(k_x, k_y, f) = (\hat{H}\bar{\hat{H}})^{-1} \Gamma_{R_e} - \Gamma_R, \quad (8)$$

where $\bar{\hat{H}}$ is the complex conjugate of \hat{H} . Besides the PSD of the noise, we are interested in the spectral signal-to-noise ratio (SSNR):

$$\text{SSNR}(k_x, k_y, f) = \frac{\Gamma_R(k_x, k_y, f)}{\Gamma_N(k_x, k_y, f)}. \quad (9)$$

In the present article, when estimating the parameters of the spectral error model, we assume that they are independent of the spatial direction and consider all spectral quantities as functions of the temporal frequency f and the spatial wavenumber

k , with $k = \sqrt{k_x^2 + k_y^2}$. To perform analyses along one dimension only (space or time) we can derive marginal PSDs and CPSDs by integrating the two-dimensional space-time PSD and CPSD along the other dimension. In this article, for easier interpretation, the results are shown as functions of wavelength $\lambda = 1/k$ and period $p = 1/f$ rather than wavenumber and frequency. In the following, the modulus of the transfer functions and the SSNRs are expressed in dB; the dB value of a dimensionless variable v is $10 \times \log_{10}(v)$.

c. Results

In this section, the parameters of the spectral error model of IMERG are identified using the GV-MRMS data as the truth. The equivalent results for CMORPH, GSMAP, PERSIANN, and for the near-real-time Early Run IMERG product, are provided as supplemental material to this article. Figure 3 shows the modulus and argument of the estimated transfer function $\hat{H}(k, f)$ of IMERG. Figure 4 shows the marginal transfer

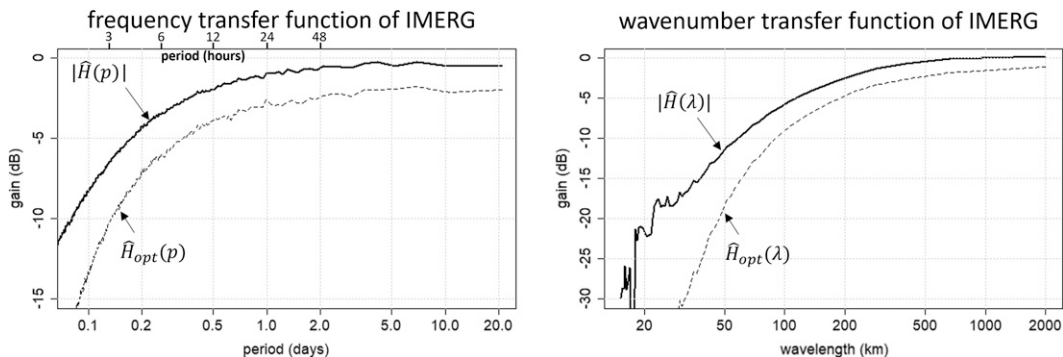


FIG. 4. Modulus of the empirical marginal transfer functions along the (left) temporal frequency and (right) spatial wavenumber dimensions of IMERG estimated against GV-MRMS from two years of data over the southeastern United States (solid line). The marginal transfer functions are obtained through Eq. (7) applied to the marginal PSD and CPSD. The dashed lines show what would be the optimal Wiener transfer function for MSE minimization (see section 5), estimated from the spectral signal to noise ratio (SSNR) of IMERG as a function of frequency and wavenumber.

functions (modulus only) along frequency and wavenumber, obtained by applying Eq. (7) with the marginal PSDs and CPSDs. A modulus (gain) of 0 dB means that the precipitation signal is not distorted at the corresponding frequency, positive dB values correspond to amplified precipitation signal (overestimated variability) and negative dB values to a dimmed signal (underestimated variability). The argument (phase) of the transfer function reveals the systematic spatial shift and temporal delays between the true and retrieved precipitation. A positive argument indicates that the retrieval is in advance in time compared to the truth (which, depending on the dominant direction of propagation of the systems, may also correspond to a systematic spatial shift). As observed from Figs. 3 and 4, at scales coarser than the 100–200-km wavelength and the 3–4-h period the gain is within the -2 to $+2$ dB range, meaning that the precipitation signal is not dramatically distorted by the retrieval process at these medium-to-large scales. However, a gain slightly higher than 0 dB at $\lambda > 300$ km and $p > 6$ h indicates that the IMERG tends to amplify the variability of precipitation at the largest scales. At wavelengths shorter than 100 km, the precipitation signal is filtered out with a gain rapidly decreasing below -3 dB and down to values lower than -15 dB. The transfer function, as it filters out or attenuates the high frequencies and wavenumbers and preserves the low ones, is therefore essentially that of a low-pass filter along both spatial and temporal dimensions.

The argument of the transfer function is close to zero at all frequencies and wavenumbers (Fig. 3, right panel), except where the gain tends toward infinitely small values (note: for infinitesimal values of the gain, the phase is undefined/random). At the short periods (< 4 h) the average phase is, however, slightly higher than 0, which reveals that when IMERG does not perfectly capture the timing of precipitation it is more likely to detect precipitation a few minutes early than late. This tendency has been documented for several satellite QPEs (Turk et al. 2009; Utsumi et al. 2019) and can be explained by the falling time of the hydrometeors between the upper cloud layers to which passive spaceborne radiometric measurements are sensitive and the near-surface gauge–radar measurements.

At the 10-km and 30-min native resolution of IMERG, the fraction τ of the error variance explained by the deterministic systematic linear filtering effect is 48%, with the remaining 52% of the error variance coming from the noise. For comparison, if we consider a systematic intensity-dependent retrieval bias (conditional bias, Kirstetter et al. 2013) instead of a filtering term, we only explain 31% of the error variance (Fig. 5, top). This is because the errors coming from the deterministic filtering appear as seemingly random (or partially random) when their dependence on frequency and wavenumber is not accounted for. Moreover, these statistics confirm that, at high resolution, the error of a satellite QPE cannot reasonably be represented as a purely random term. However, because the systematic filtering effect predominantly affects the high frequencies and wavenumbers, the relative weight of systematic errors in the error budget of IMERG decreases when aggregating the data at coarser resolutions. At the 50-km and 2-h resolution for example, $\tau = 19\%$, and the intensity-dependent mean bias only explains 3% of the error variance (Fig. 5, bottom). The fact that the magnitude of

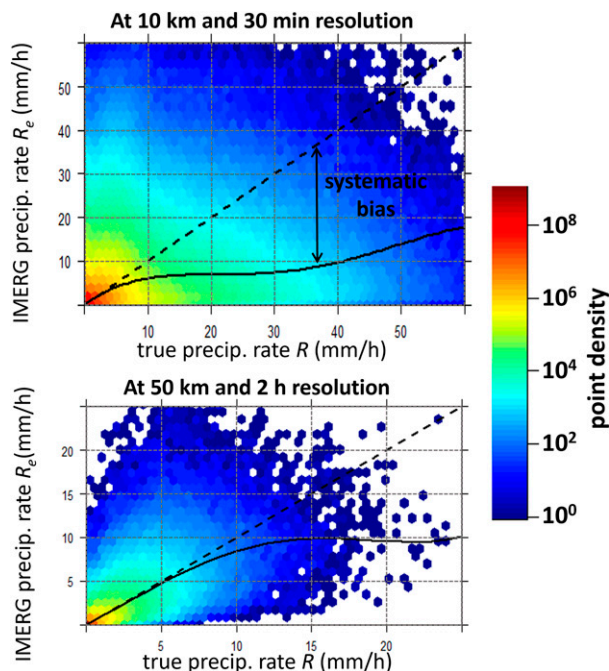


FIG. 5. IMERG precipitation rate R_e against the “true” GV-MRMS precipitation rate R (top) at 10-km and 30-min resolution and (bottom) at 50-km and 2-h resolution. In both panels, the difference between the 1:1 identity line (dashed line) and the expected conditional IMERG precipitation rate $E[R_e|R]$ (solid line, fitted as a fourth-order polynomial) shows the systematic bias as a function of precipitation intensity. At the 10-km and 30-min resolution, the residual variance of the polynomial fit is 69% of the variance of error $R_e - R$, which means that the systematic bias $E[R_e|R] - R$ explains 31% of the error variance. At the 50-km and 2-h resolution, the residual variance is 97% of the variance of the error.

the conditional mean bias decreases at coarser resolutions is an indication that this bias is in fact a direct consequence of the low-pass filtering. This is confirmed by Fig. 6, which shows that, at the 10-km and 30-min resolution, the linear filtering term H , while regressed as a function of frequency and wavenumber and not as a function of precipitation intensity, actually explains 100% of the observed systematic intensity-dependent bias. Indeed, the polynomial fit of $E[R_e|H * R]$ follows perfectly the 1:1 line, revealing that there is no remnant intensity-dependent bias in IMERG after the filtering effect is accounted for. We note that the systematic term in our model only accounts for linear filtering effects (which can include systematic multiplicative or additive biases); if nonlinear filtering effects also exist, their contribution to the error will be reported on the random term.

Turning our focus now on the random error term, Fig. 7 compares the space–time PSD of the noise [derived from Eq. (7)] with the PSD of the “true” precipitation signal. Figure 8 compares the marginal PSDs. If we focus on periods longer than 6 h and wavelengths longer than 100 km, we see that the magnitude of the noise does not change with the period $p = 1/f$ (temporally white noise). In this wavelength and period range, the magnitude of the noise slightly increases with the wavelength $\lambda = 1/k$ with a dependence of the form $\Gamma_N \approx \alpha k^{-0.6}$ (spatially pink noise). In

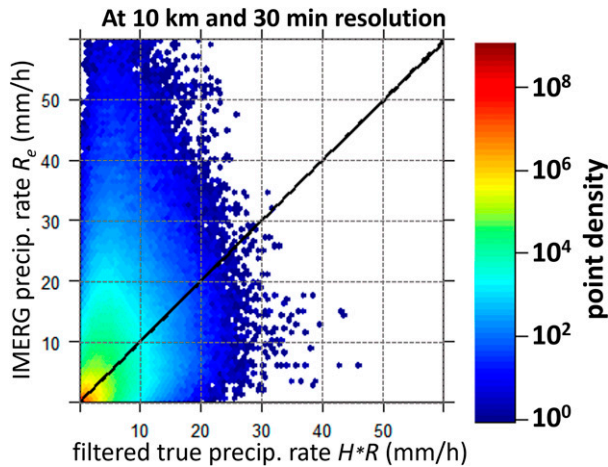


FIG. 6. IMERG precipitation rate R_e against the filtered GV-MRMS precipitation rate $H * R$ at 10-km and 30-min resolution. The filtering term H applied here to GV-MRMS mimics the systematic filtering effect of the IMERG retrieval. The black line shows the expected conditional IMERG precipitation rate $E[R_e|H * R]$ fitted as a fourth-order polynomial.

the same range of wavelengths and periods, the PSD of the precipitation signal increases with both wavelength and period; while the dependence on period does not appear to be log linear, the dependence on the wavelength is approximately of the form $\Gamma_R \approx \alpha k^{-1.5}$. Consequently, the SSNR tends to increase with wavelengths ($SSNR \approx \alpha k^{-0.9}$) and period (non-log-linear dependence); it is consistently around or above 0 dB in this wavelength and period range, meaning that the magnitude of the precipitation signal is at least as high as the magnitude of the noise. The periods shorter than 6 h and wavelengths shorter than 100 km appear to follow a totally different noise regime. This range of wavelengths and periods is characterized by high levels of noise, with a SSNR below -1 dB. While the PSD of the precipitation signal decreases continuously with shorter wavelengths, for $\lambda < 100$ km and $p < 6$ h the PSD of the noise follows an opposite trend, eventually leading to an extremely low SSNR (between -30 and -90 dB) at the finest accessible spatial and temporal scales. This “pseudo-blue” noise regime (i.e., PSD of the noise increasing

with wavenumber) is likely coming from mislocation errors in the retrieved precipitation fields and the associated “double-penalty” phenomenon (Rossa et al. 2008) which causes errors of opposite sign to be frequently found in a close vicinity.

The PSD of the noise shown in Figs. 7 and 8 is computed as an average over two years of data and over the whole 2 million km² study domain. The noise is, however, expected to be nonstationary and its PSD is expected to be highly variable across space and time and locally related to the PSD of the precipitation (even if the two variables are linearly independent by definition). For the implementation of the error model, we therefore chose to parameterize the SSNR instead of the PSD of noise (in addition to the parameterization of the transfer function). The parameterization is made in the wavelet domain (see appendix; Kumar and Foufoula-Georgiou 1997; Cottis et al. 2016) instead of the Fourier domain, using a discrete 3D Haar wavelet transform, because discrete wavelets provide a “natural” discrete decomposition of the frequency–wavenumber space, leading to a finite number of frequency-and-wavenumber bands. The gain of the transfer function and the SSNR are assumed to be constant within each one of the frequency-and-wavenumber bands resulting from the discrete wavelet decomposition. Assuming a constant SSNR is equivalent to assuming that the local PSD of the noise scales linearly with the local PSD of precipitation within each frequency-and-wavenumber band.

The principal advantage of using a spectral error model when compared to classical intensity-dependent error models is the ability to account for the spatial and temporal correlation of the noise and of the precipitation signal itself, to eventually provide a prediction of the uncertainty not only at the pixel scale, but also at any aggregated space–time scale. After deriving the local PSD of the noise from the local PSD of R_e using the previously estimated SSNR parameters and a maximum-overlap wavelet transform (see appendix) for robust estimation of the local PSD, we can estimate its local variance (or standard deviation) at the desired scale by integrating its PSD from the zero frequency and zero wavelength to the chosen frequency and wavelength. Finally, at the desired location and time, and at the desired scale, the local variance of the error $\sigma_{err}^2 = \text{var}(R_e - R)$ is computed as the sum of the local residual noise variance after filtering $\text{var}(H * N)$ and the local variance

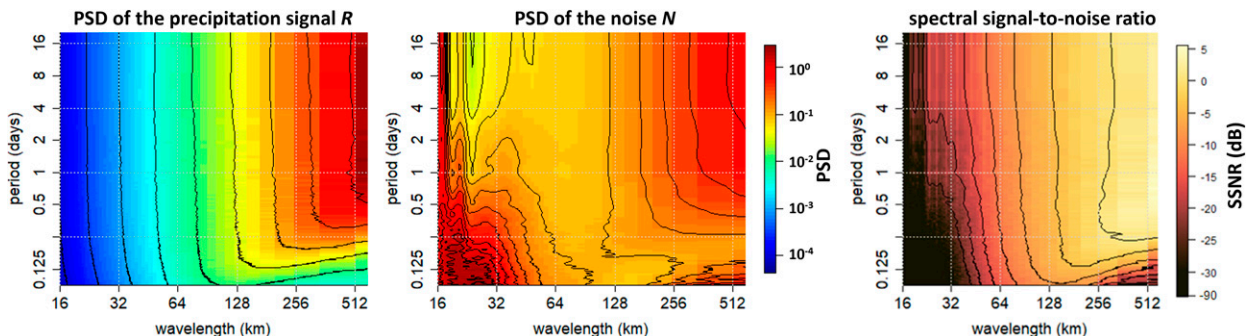


FIG. 7. (left) Power spectral density of the “true” precipitation signal R computed from two years of GV-MRMS data over the southeastern United States. (center) Power spectral density of the noise N for the IMERG product estimated for the same region and period. (right) Spectral signal-to-noise ratio. Smoothed isocontours are added over the colormaps to improve visualization.

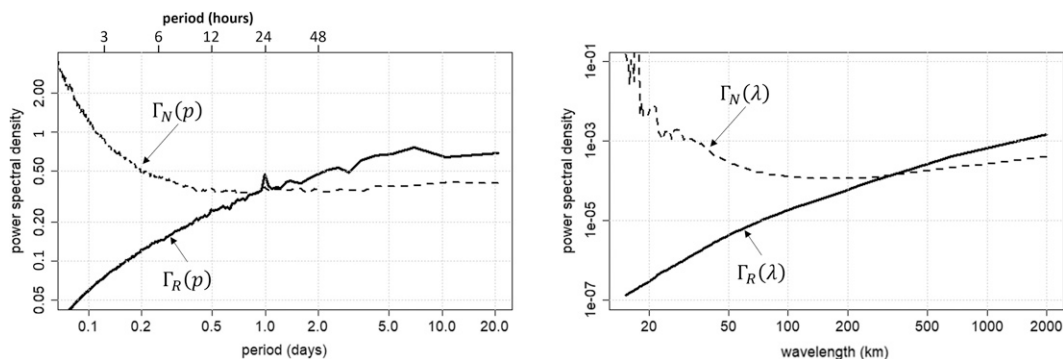


FIG. 8. Marginal power spectral density of the noise N of IMERG (dashed line) compared to the PSD of the “true” GV-MRMS precipitation signal R (solid line), along the (left) temporal frequency and (right) spatial wavenumber dimensions; computed from two years of data over the southeastern United States. The spatial and temporal power spectra of the noise are not monotonic, revealing the existence of different noise regimes at different scales.

of the precipitation signal lost due to the systematic filtering term $\text{var}[(H * R) - R]$. Figure 9 shows maps of the predicted standard deviation σ_{err} of the IMERG error around longitude 99°W and latitude 33°N , at 1945 UTC 7 January 2018, at the native 10-km and 30-min resolution of IMERG (Fig. 9c), and at the coarsened resolution 40 km and 2 h (Fig. 9d). As

expected, the predicted uncertainty, quantified as the standard deviation of the error, decreases with space–time coarsening, however, with a spatially heterogeneous rate and not as rapidly as would be the case for a white noise.

From Fig. 9b we can see that the predicted standard deviation of the error σ_{err} does not depend only on the precipitation

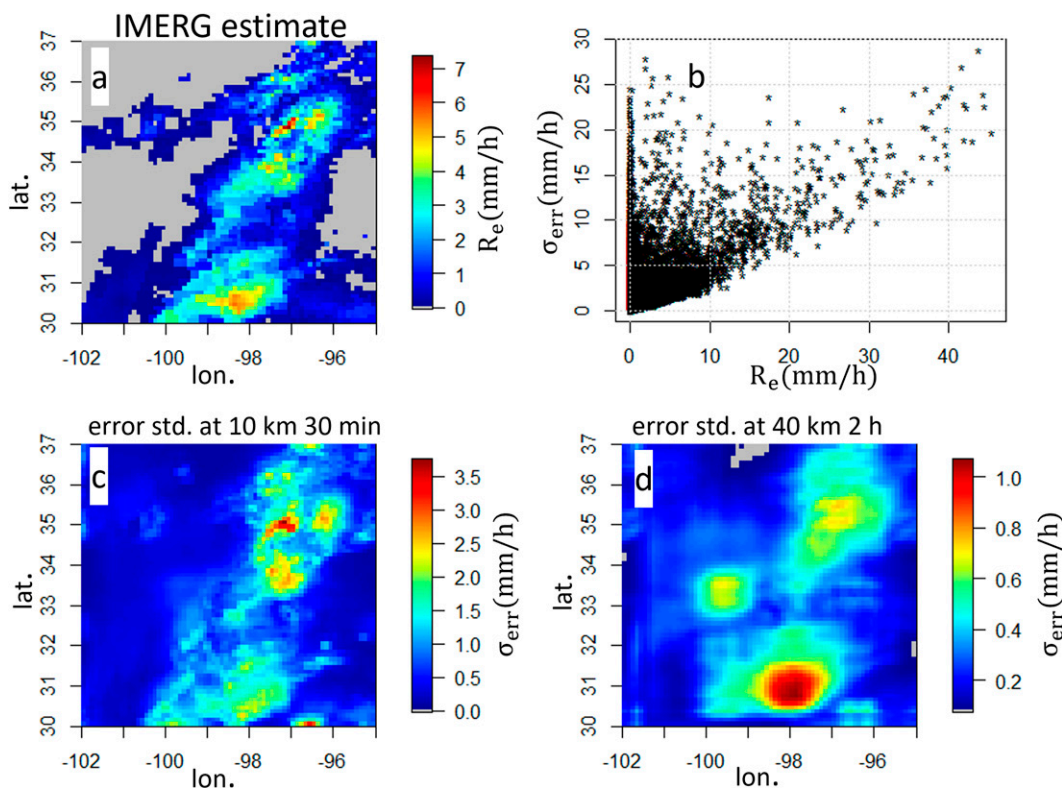


FIG. 9. (a) IMERG retrieved precipitation intensity between longitudes 95° and 102°W and latitudes 30° and 37°N , for the 30-min period centered at 1945 UTC 7 Jan 2018. (b) Scatterplot of the predicted standard deviation of the IMERG error from the spectral model vs IMERG estimated precipitation intensity at 10-km and 30-min resolution, for the same area as in (a), from 1900 UTC 6 Jan 2018 to 2130 UTC 8 Jan 2018. (c) Map of the predicted standard deviation of the IMERG error at 10-km and 30-min resolution at 1945 UTC 7 Jan 2018. (d) Map of the predicted standard deviation of the IMERG error at 40-km and 2-h resolution at 1945 UTC 7 Jan 2018.

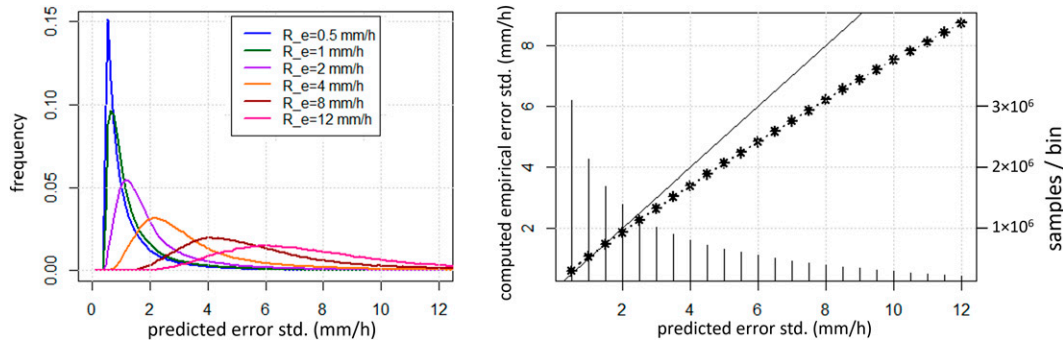


FIG. 10. (left) Distributions of the predicted standard deviation σ_{err} of the IMERG error at 10-km and 30-min resolution for different values of the IMERG precipitation intensity R_e (with a $\pm 3\%$ tolerance range on the R_e values), highlighting the relatively large dispersion of σ_{err} for a given value of R_e , and in particular for large R_e values. (right) Computed empirical standard deviation of the IMERG error at 10-km and 30-min resolution (against the GV-MRMS truth) as a function of the predicted standard deviation of the error from the spectral model (dots); the vertical bars show the number of samples used to compute the empirical standard deviation in each bin; the solid diagonal line is the 1:1 identity line. In both panels, statistics are computed over the full $1200 \text{ km} \times 1900 \text{ km} \times 2 \text{ yr}$ dataset.

intensity as would be the case for classical error models. Because in our case the predicted uncertainty is driven by the local PSD of precipitation, we can have $R_e(x_1, y_1, t_1) = R_e(x_2, y_2, t_2)$ and $\sigma_{\text{err}}(x_1, y_1, t_1) \neq \sigma_{\text{err}}(x_2, y_2, t_2)$. Specifically, if the local variability of precipitation is stronger around the location (x_1, y_1, t_1) than around the location (x_2, y_2, t_2) , then $\sigma_{\text{err}}(x_1, y_1, t_1) > \sigma_{\text{err}}(x_2, y_2, t_2)$. The left panel of Fig. 10 shows the distribution of the predicted error standard deviation at IMERG’s native resolution, over the whole $1200 \text{ km} \times 1900 \text{ km} \times 2 \text{ yr}$ study area and period, for different values of the IMERG precipitation intensity R_e . While the predicted error standard deviation increases in average with the precipitation intensity, a relatively large dispersion of σ_{err} can be observed for a given value of R_e , and in particular for the large R_e values. The right panel of Fig. 10 shows the empirical standard deviation of the error $R_e - R$ of IMERG against GV-MRMS versus the predicted σ_{err} of IMERG from the spectral model (considering all values of R_e together). We can see that, over a large sample set, the empirical standard deviation increases with the predicted standard deviation and that the model can accurately predict the error standard deviation up to 4 mm h^{-1} . We note, however, that the model tends to overestimate large values of σ_{err} ($> 4 \text{ mm h}^{-1}$), likely because it assumes that the SSNR is independent from the precipitation intensity. In addition, Fig. 11 shows that, for several specific values of the IMERG precipitation intensity R_e between 0.5 and 12 mm h^{-1} , the spread of the empirical distributions of the errors $R_e - R$ increases with the predicted standard deviation.

4. Variability of the model parameters, nonstationarity, and heteroscedasticity

In the previous section the parameters of the spectral error model were estimated from two years of data over a 2 million km^2 area. Using constant parameters, the spectral error model is expected to produce reasonable predictions of the uncertainty when considering a large set of estimates that are statistically representative of the average climatic, environmental, and observational conditions corresponding to the data use for

the calibration. However, the optimal parameters of the error model are likely to vary with climate regimes, seasons, and precipitation types. To evaluate the ability of the spectral error model to always produce reasonable estimates of the uncertainty of the QPE under all possible conditions, and to determine to which degree a dynamical and adaptive parameterization would eventually be necessary, we explore here the variability of the relationships between $\hat{R}(k, f)$, $\hat{H}(k, f)$, and $\hat{N}(k, f)$ over our study area and period.

Figure 12 shows how variable the marginal transfer functions $\hat{H}(f)$ and $\hat{H}(k)$ are when computed over subsets of the available data. We computed a total of 9345 empirical “local” transfers functions over $600 \text{ km} \times 600 \text{ km} \times 64 \text{ h}$ blocks of data belonging to the $1200 \text{ km} \times 1900 \text{ km} \times 2 \text{ yr}$ dataset. Of concern here is how wide the distributions, as indicated by the various quantile lines, are at different frequencies and wavenumbers. The marginal transfer functions have a small spread in gain at large scales ($p > 6 \text{ h}$, $\lambda > 100 \text{ km}$) with a maximum of 3-dB difference between the 15% and 85% quantiles. At shorter periods and wavelengths, the gain is consistently below -3 dB ; it is, however, proportionally more variable, with up to 10-dB difference between the 15% and 85% quantiles.

Figure 13 shows the variability of the marginal PSDs of the noise and of the SSNR. One can see that the PSD of the noise is highly variable with at least an order of magnitude between the 15% and 85% quantiles at all frequencies and wavelengths. The SSNR, is found to have a smaller spread, with a difference around 3–5 dB between the 15% and 85% quantiles, except for the very short wavelengths and periods ($p < 2 \text{ h}$, $\lambda < 50 \text{ km}$) where the difference goes up to 15 dB. While the reliance on a static parameterization of the SSNR is clearly a limitation of the spectral error model, it is still far more reasonable than assuming constant PSD of the noise (i.e., variability of noise is constant at all scales).

Arguably, while the transfer function is more dependent on the observation system itself (i.e., instrument resolution, sampling rate, etc.), the noise level is more dependent on environmental parameters (e.g., the background emissivity of Earth’s surface).

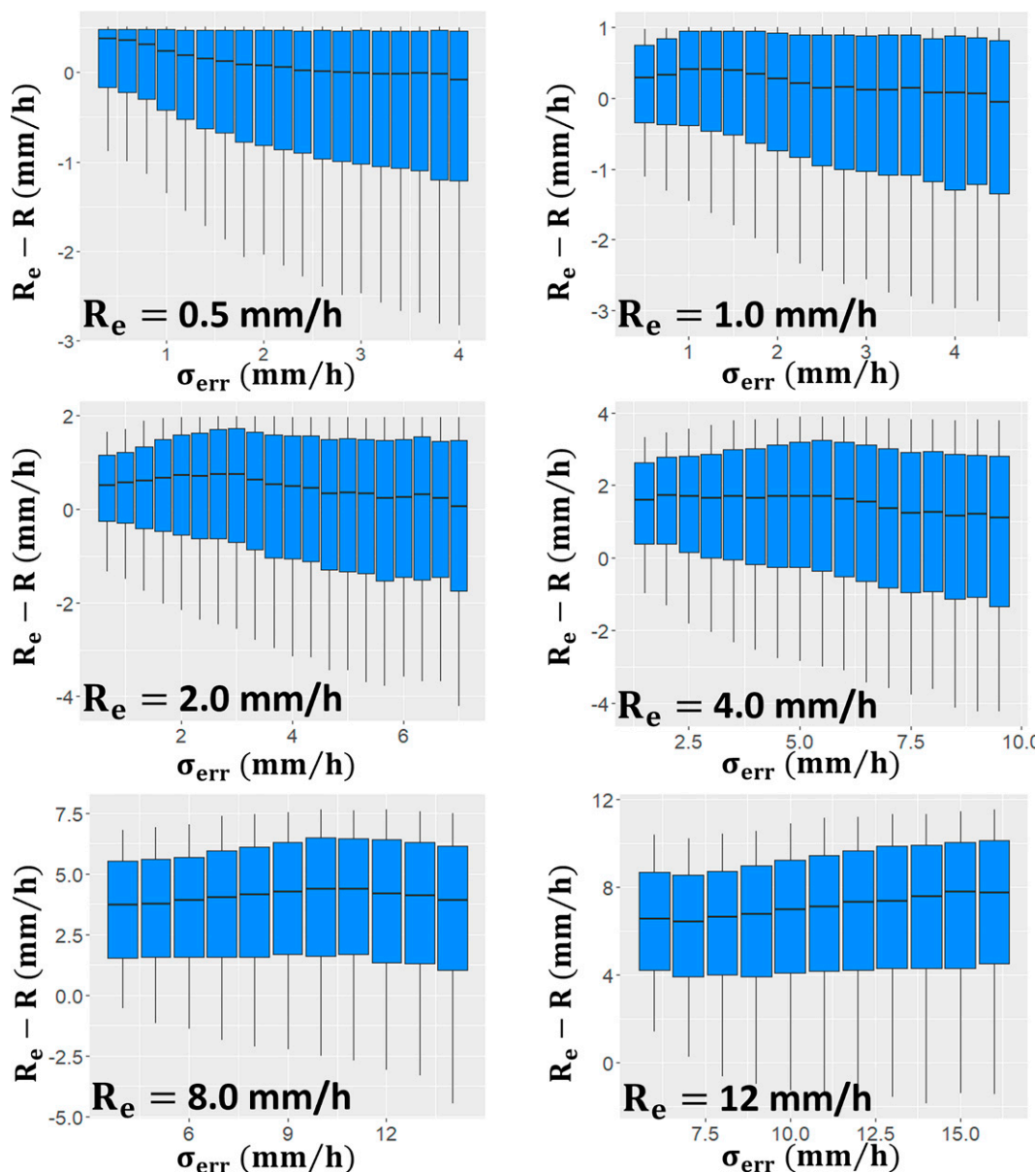


FIG. 11. Empirical distribution of the errors $R_e - R$ as a function of the predicted standard deviation of the error σ_{err} for different values of the IMERG precipitation intensity R_e (with a $\pm 3\%$ tolerance range on the R_e values). The boxes range from the 25th to the 75th percentile and the whiskers from the 10th to the 90th percentile, the horizontal lines mark the median. Each box is computed from at least 2000 samples.

This is illustrated in Fig. 14, which shows the climatic variability of the transfer function and the SSNR when computed over two different climatic regions, namely, Oklahoma and northeastern Texas ($30^\circ\text{--}37^\circ\text{N}$, $95^\circ\text{--}102^\circ\text{W}$) and the Appalachian Mountains ($35^\circ\text{--}42^\circ\text{N}$, $78^\circ\text{--}85^\circ\text{W}$). It shows strong stability of the transfer function across these two regions with different climates. The SSNR, however, varies significantly across the two regions and is found to be 1–3 dB lower in the Appalachian Mountains compared to the Oklahoma and northeastern Texas region at all periods longer than 6 h and all wavelengths longer than 100 km. This is consistent with many previously published studies

showing that precipitation in mountainous areas is particularly challenging for satellite QPEs (Barros and Arulraj 2020). We note, however, that the geographical climatic variability only explains a small fraction of the event-to-event variability shown in Figs. 12 and 13.

In terms of heteroscedasticity, while a dependence between the local PSD of the noise and the local PSD of the true precipitation certainly exists, the results presented here and in Guilloteau and Foufoula-Georgiou (2020) and Guilloteau et al. (2021) suggest that this relation is not perfectly linear, i.e., that the SSNR varies with precipitation intensity. The results

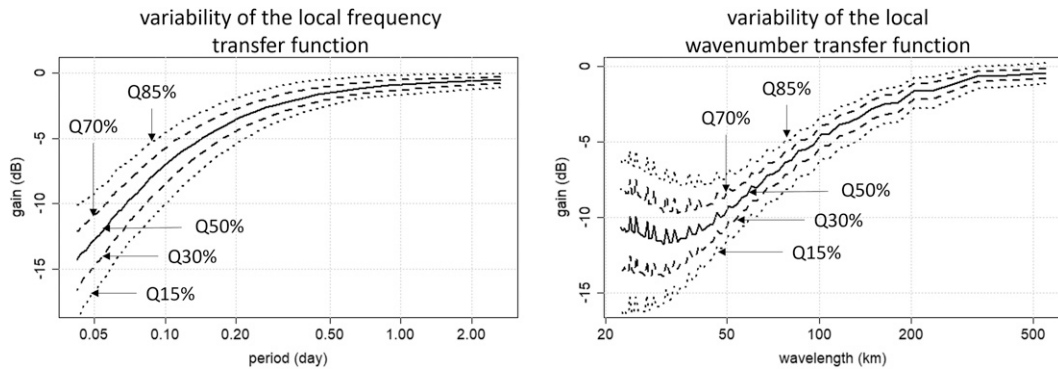


FIG. 12. Variability of the IMERG “local” transfer functions across time and space. Median, 15%, 30%, 70%, and 85% quantiles of the marginal transfer functions as functions of the (left) frequency and (right) wavenumber, computed from $600 \text{ km} \times 600 \text{ km} \times 64 \text{ h}$ subsets of the $1200 \text{ km} \times 1900 \text{ km} \times 2 \text{ yr}$ available dataset.

of Guilloteau et al. (2021) and several other published studies (Tian et al. 2013; Maggioni et al. 2016; You et al. 2020) seem to indicate that the SSNR of satellite QPEs actually increases on average with the spectral power (magnitude) of the precipitation signal. This is corroborated by the fact that our spectral model tends to overestimate large σ_{err} values when using the constant SSNR hypothesis (Fig. 10, right). Figure 15 further confirms the existence of nonlinear relationships between the magnitude of the precipitation signal and the standard deviation of the noise

in the wavelet domain. Because the wavelet coefficients are the result of a bandpass filtering in the Fourier domain, they characterize the local variations of the signal in a specific frequency–wavenumber band. Therefore, comparing the magnitude of the wavelet coefficients $W_N(x, y, t)$ derived from the noise $N(x, y, t)$ to the magnitude of the wavelet coefficients $W_R(x, y, t)$ derived from $R(x, y, t)$ is equivalent to comparing the local value of the PSDs of N and R in the corresponding frequency–wavenumber band. The wavelet filter used for Fig. 15

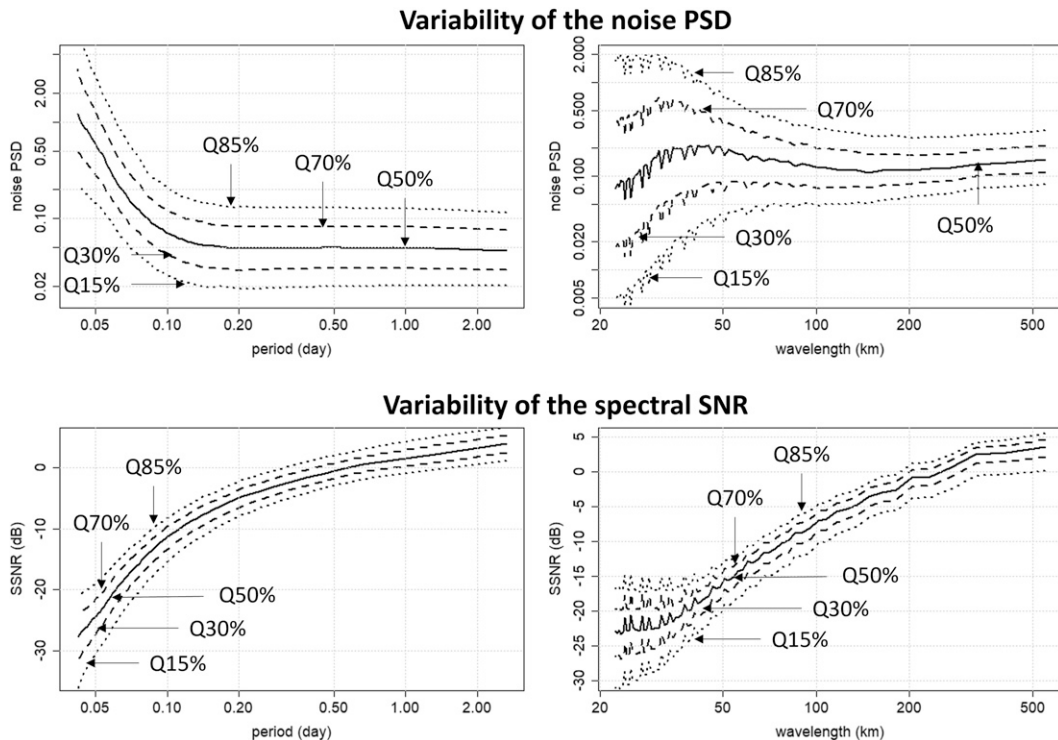


FIG. 13. Variability of the PSD (top) of the noise and (bottom) of the SSNR of IMERG across time and space. Median, 15%, 30%, 70%, and 85% quantiles of the PSD of the noise and of the SSNR as functions of the (left) temporal period and (right) spatial wavelength. Individual PSDs computed over $600 \text{ km} \times 600 \text{ km} \times 64 \text{ h}$ subsets of the $1200 \text{ km} \times 1900 \text{ km} \times 2 \text{ yr}$ available dataset.

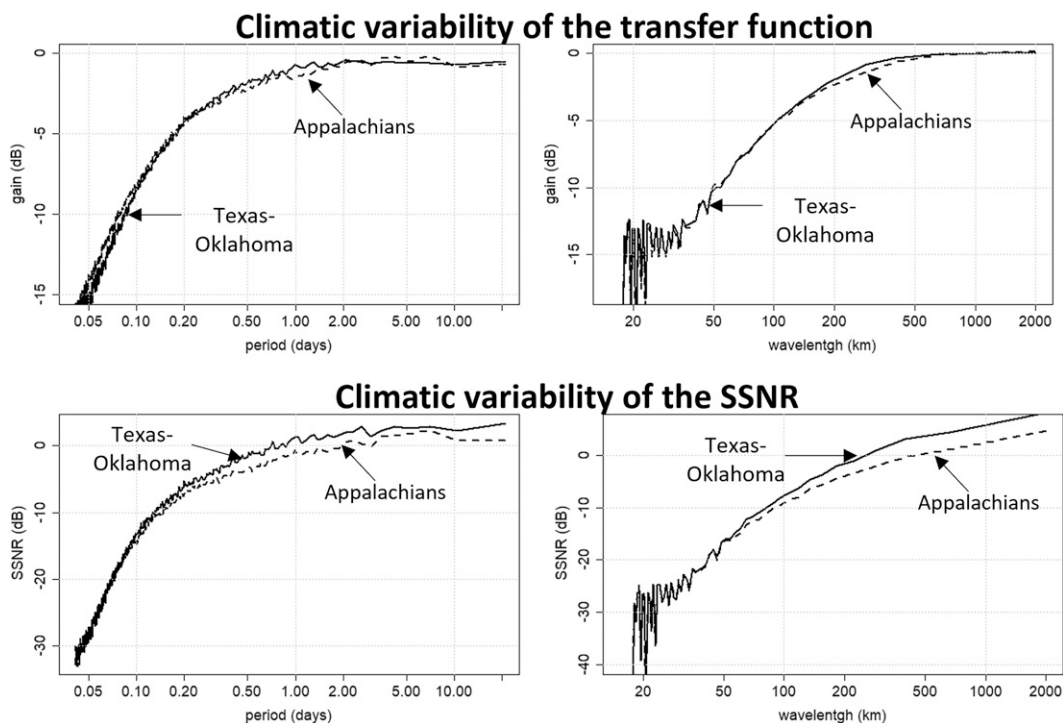


FIG. 14. Variability (top) of the transfer function and (bottom) of the SSNR of IMERG across two different climatic regions, namely, Oklahoma and northeastern Texas (30° – 37° N, 95° – 102° W; solid line) and the Appalachian Mountains (35° – 42° N, 78° – 85° W; dashed line). The transfer functions and SSNR functions are computed from two years of data.

is a “Daubechies 8” 3D filter (Cohen et al. 1992; Whitcher 2020) centered on the frequency $f = 1/4 \text{ h}^{-1}$ and on the wavenumber $k = 1/200 \text{ km}^{-1}$. Figure 15 confirms that the local PSD of the noise scales with the local PSD of the precipitation signal, but also reveals that this scaling is not perfectly linear and that the SSNR tends to increase with higher magnitude of the precipitation signal. Eventually, while assuming constant SSNR (i.e., linear scaling) for given f and k may be a rough approximation, the feasibility and pertinence of defining a parametric representation of the SSNR as a function of k , f , and of the local magnitude of the PSD of precipitation $\Gamma_R(k, f)$ would eventually be driven by the volume of data necessary to perform the parameter estimation without overfitting.

5. Discussion, implications for QPE evaluation, and multisource merging

It was found herein that, for the IMERG QPE, and for all other analyzed multisatellite QPEs (see supplemental material), the transfer function $\hat{H}(k, f)$ is essentially a low-pass filter. This can be partially attributed to the error-minimization procedures used in the retrieval algorithms. From signal processing theory, the mean squared error (MSE) caused by an additive noise can be minimized by the Wiener optimal filter (Wiener 1949; Vaseghi 2008; Daliakopoulos and Tsanis 2012) of the form

$$\hat{H}_{\text{opt}}(k, f) = \frac{\Gamma_R(k, f)}{\Gamma_R(k, f) + \Gamma_N(k, f)}. \quad (10)$$

Even if the retrieval algorithms are not necessarily explicitly designed following the Wiener optimal filtering theory, the actual transfer functions of the QPEs are found here to be relatively close to the Wiener optimal transfer functions (see Fig. 4 for IMERG). This is not surprising, as a QPE designed to have minimal MSE is expected to filter out the fine spatial and temporal scales at which the noise level is high.

The dependence of the retrieval error on frequency and wavenumber, and the existence of a systematic filtering effect have important consequences in terms of QPE evaluation, comparison, and product merging. One first consequence is that, because of the systematic filtering term H , the error is not independent from the true precipitation signal R , and therefore, the hypothesis of additive and mutually orthogonal errors across different QPEs is not valid in general. Indeed, when considering the decomposition of the retrieval error given by Eq. (3), the term $(H * R) - R$ is expected to be correlated across different QPEs, even when those are derived from totally independent sources. The linear correlation across the errors of different QPEs may in fact be relatively high considering that most QPEs are expected to have similar low-pass transfer functions; and it is expected to be more pronounced at high resolutions where the effect of the low-pass filtering is the strongest (see Fig. 5). This effect may arise not only when comparing two satellite QPEs but also when comparing a satellite QPE to interpolated gauge data. Indeed, most gauge precipitation datasets utilize smooth interpolation techniques which effect is similar to that of low-pass filtering. The issue of

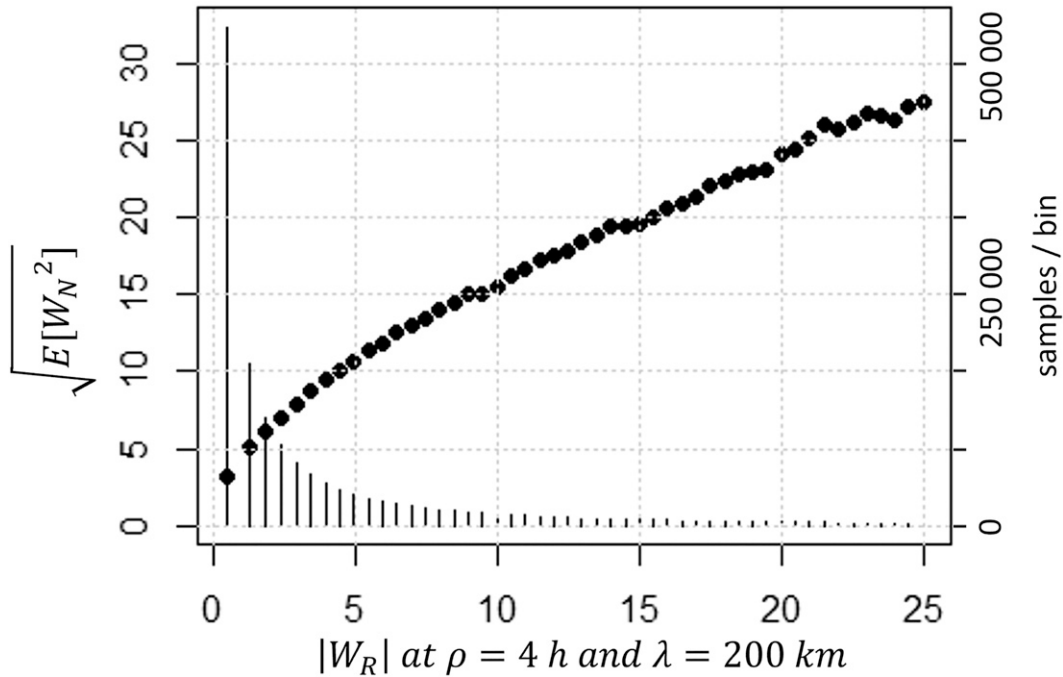


FIG. 15. Standard deviation (dots) of the wavelet coefficients W_N at $f = 1/4 \text{ h}^{-1}$ and $k = 1/200 \text{ km}^{-1}$ derived from the noise $N(x, y, t)$ of IMERG estimates against the absolute value of the wavelet coefficients W_R derived from the GV-MRMS truth $R(x, y, t)$. Wavelet coefficients are the result of a bandpass filtering of the signal, they characterize the local signal variations in a specific frequency-wavenumber band. A 3D “Daubechies 8” wavelet is used here; high-order Daubechies wavelets are practical for their narrow bandwidth. The vertical bars show the number of samples used to compute the standard deviation in each bin. The full $1200 \text{ km} \times 1900 \text{ km} \times 2 \text{ yr}$ dataset is used here.

nonorthogonal errors across products is particularly critical when using techniques such as total least squares or triple collocation for QPEs evaluation (e.g., Alemohammad et al. 2015; Li et al. 2018; Lu et al. 2021), and more generally when ranking QPEs based on their consistency with supposedly “independent” data. For example, a QPE that would correctly reproduce the fine-scale variability of precipitation may show seemingly poor performance when compared to smoothly interpolated gauge data, and a QPE that would filter out the fine-scale variability would misleadingly show higher consistency with this smoothly interpolated gauge data.

Nonadditive and nonorthogonal errors across products also have important consequences in terms of product merging, as inverse error variance weighting (e.g., Huffman et al. 1995; Mastrantonas et al. 2019) is no more an optimal minimum MSE solution in that case. With our proposed representation of the error, if we have m estimates R_i such as

$$R_i = H_i * (R + N_i) \tag{11}$$

with i in $\{1, 2, \dots, m\}$, $E[N_i] = 0$, $\Gamma_{N_i, R} = 0$, and $\Gamma_{N_i, N_j} = 0$ if $i \neq j$, the linear combination:

$$R_{\text{opt}} = \sum_{i=1}^m G_i * R_i \tag{12}$$

has a minimal mean squared error $E[(R_{\text{opt}} - R)^2]$ when

$$\hat{G}_i = \frac{\overline{\hat{H}_i}}{|\hat{H}_i|^2} \times \frac{1}{\Psi \Gamma_{N_i}} \times \frac{\Gamma_R}{\Gamma_R + \Psi^{-1}}, \tag{13}$$

with

$$\Psi = \sum_{j=1}^m \frac{1}{\Gamma_{N_j}}. \tag{14}$$

The first term of Eq. (13), which is the inverse of the transfer function of each individual estimate, is necessary to suppress the linear dependences across the errors of the different estimates before merging.

We note that our model cannot provide the full statistical distribution of the errors if the characterization of the noise is limited to its PSD (as the PSD only characterizes the order-two moment). One may explore the higher-order spectra of the noise from the data, which is always possible after having estimated the transfer function \hat{H} , or assume a given parametric distribution, as long as it can be defined by its first two moments (we recall that, by definition, $E[N] = 0$).

The spectral error model proposed here can serve as a basis to generate ensembles of possible precipitation fields for the QPEs.

For this purpose, one shall consider the “inverse” system corresponding to the equation: $R(x, y, t) = H_{\text{inv}}(x, y, t) * [R_e(x, y, t) + N_{\text{inv}}(x, y, t)]$. Once \hat{H}_{inv} and $\Gamma_{N_{\text{inv}}}$ are identified, the ensemble generation simply consists in drawing multiple realizations of the noise $\{N_{\text{inv},i}\}$ with the $\Gamma_{N_{\text{inv}}}$ PSD and applying the convolution operator H_{inv} to the sum $R_e + N_{\text{inv},i}$. This ensemble generation approach will impose in particular that each ensemble member preserves the space–time PSD of the true precipitation (see [Guiloteau et al. 2018](#)).

6. Conclusions

The results presented in [Guiloteau et al. \(2021\)](#) exposed the fact that the spectral properties of the retrieval errors in the evaluated satellite QPEs are incompatible with the representation of the error provided by most of the classical error models, which do not account for the dependence on the spatial wavenumber and temporal frequency. To formally account for this dependence, we introduced a spectral error model that is general and thus applicable to any QPE product. The model describes the retrieved precipitation as the result of applying a deterministic space–time filtering operator to the sum of the “true” precipitation signal and a random noise. The model is parameterized in the Fourier domain, the transfer function of the space–time filter and the PSD of the noise are directly estimated from data.

For IMERG and the other assessed multisatellite QPEs (in supplemental material), the transfer function is found to be that of a low-pass filter along both spatial and temporal dimensions, which was expected considering the existing limitations in terms of instrument resolution and temporal sampling of the observations, as well as the (dynamic) interpolation and error minimization procedures, as for example the Kalman filters used in several multisatellite QPE algorithms ([Ushio et al. 2009](#); [Joyce and Xie 2011](#)). While most of the previously published analyses of errors in satellite QPEs, which did not account for the frequency and wavenumber dependence of the systematic errors, found that random errors broadly dominate the error budget (e.g., [AghaKouchak et al. 2012](#); [Maggioni et al. 2016](#); [Tang 2020](#)), here we found that the deterministic filtering term, which represents systematic distortions of the precipitation signal, explains nearly half (48%) of the error variance of IMERG at its native 10-km and 30-min resolution. We note that a nonlinear systematic filtering term could potentially explain an even greater fraction of the error variance; however, the identification of nonlinear systems in the Fourier domain is far from trivial. By highlighting the existence of systematic frequency-and-wavenumber-dependent distortions of the precipitation signal in QPEs, our model calls for caution when performing evaluation, comparison and merging of precipitation estimates from independent sources, as it implies that the hypothesis of mutually orthogonal errors across QPEs is generally not verified.

After having characterized the transfer function $\hat{H}(k, f)$ and the PSD of the noise $\Gamma_N(k, f)$ we are able to derive, via localized wavelet-based analysis, an estimate of the local variance of the retrieval error from the local PSD of the retrieved precipitation at any location and time, and at any desired spatial and temporal resolution. By deriving the local PSD of the noise from the local

PSD of the retrieved precipitation, our model can handle the nonstationarity of precipitation and the resulting heteroscedasticity. However, within the study area, the SSNR, which is used to relate the PSD of the noise to the PSD of the precipitation signal, was not found to be identical over different regions eventually calling for a dynamical adaptive parameterization.

As for any data-calibrated error model, the most challenging question in view of global application is the generalization of the regionally learned parameters. We note in particular that only precipitation over land has been considered in the present article. The SSNR, and potentially the transfer function, are expected to be significantly different over ocean from what they are over land; the main difficulty over ocean is, however, to find a reliable reference dataset for the model calibration. Future work will explore the environmental factors that locally drive the variability of the spectral error model parameters, as well as their dependence on the instantaneous configuration of the constellation of observing sensors for multisatellite products ([Chambon et al. 2013a](#); [Kidd et al. 2021](#); [Ayat et al. 2021](#); [Rajagopal et al. 2021](#)), to eventually provide accurate estimates of the local variance of the retrieval error at any location of the globe. In particular, the convective available potential energy and the elevation are among the environmental parameters which are likely to be influential; concerning the observational parameters, the delay between two successive overpasses of microwave sensors over the region and period of interest is expected to be one of the determinant factors.

Acknowledgments. This research was supported by NASA through the Global Precipitation Measurement program (Grants 80NSSC22K0597, 80NSSC19K0684, 80NSSC19K068, 80NSSC19K0681, and WBS-573945.04.80.01.01) and the Ground Validation Program (Grants NNX16AL23G and 80NSSC-21K2045). The National Science Foundation (NSF) supported this research under the EAGER program (Grant ECCS-1839441) and the TRIPODS+X program (Grant DMS-1839336).

Data availability statement. Part of the GV-MRMS data ([Kirstetter et al. 2018](#)) used in this study is available at <https://doi.org/10.5067/GPMGV/MRMS/DATA101>. The satellite products are publicly available: IMERG-Final ([Huffman et al. 2019b](#)) at <https://doi.org/10.5067/GPM/IMERG/3B-HH/06>, IMERG-Early ([Huffman et al. 2019c](#)) at <https://doi.org/10.5067/GPM/IMERG/3B-HH-E/06>, CMORPH ([Xie et al. 2019](#)) at <https://doi.org/10.25921/w9va-q159>, GSMaP ([Ushio et al. 2009](#)) at <https://sharaku.eorc.jaxa.jp/GSMaP>, and PERSIANN-CCS ([Hong et al. 2004](#)) at <https://chrdata.eng.uci.edu>.

APPENDIX

Power Spectral Density and Cross-Power Spectral Density Estimation

Numerous methods exist for the estimation of PSDs and CPSDs in one or several dimensions. These methods can be broadly separated into two categories: parametric and nonparametric. In the present study, nonparametric approaches, which are generally simpler to use and produce robust estimates with

large datasets, are used. A parametric approach would be preferably used with a more limited amount of data or with discontinuous data (such as gauge measurements). The Welch method (Welch 1967) was used to compute the 1D marginal (cross-)spectra (Figs. 4, 8, 12, 13, and 14) and the “regional” 3D (cross-)spectra (Figs. 1, 3, and 6). The Welch method simply consists in computing PSDs and CPSDs over predefined overlapping space–time windows using a discrete Fourier transform (DFT) and averaging them. The “local” 3D spectra (Figs. 9 and 10) were estimated using a 3D maximum-overlap discrete Haar wavelet (Subramani et al. 2006; Zhang 2018; Whitcher 2020). The local PSD at a given scale is computed as the local variance of the wavelet coefficients at the corresponding scale. In addition to allow a robust estimation of the local PSD, discrete wavelets provide a “natural” discretization of the Fourier frequency–wavenumber domain, allowing to represent the PSD with a reduced number of coefficients corresponding to an equivalent number of frequency–and-wavenumber bands.

REFERENCES

- AghaKouchak, A., A. Mehran, H. Norouzi, and A. Behrangi, 2012: Systematic and random error components in satellite precipitation data sets. *Geophys. Res. Lett.*, **39**, L09406, <https://doi.org/10.1029/2012GL051592>.
- Alemohammad, S. H., K. A. McColl, A. G. Konings, D. Entekhabi, and A. Stoffelen, 2015: Characterization of precipitation product errors across the United States using multiplicative triple collocation. *Hydrol. Earth Syst. Sci.*, **19**, 3489–3503, <https://doi.org/10.5194/hess-19-3489-2015>.
- Andricevic, R., and E. Foufoula-Georgiou, 1991: A transfer function approach to sampling network design for groundwater contamination. *Water Resour. Res.*, **27**, 2759–2769, <https://doi.org/10.1029/91WR01391>.
- Ayat, H., J. P. Evans, and A. Behrangi, 2021: How do different sensors impact IMERG precipitation estimates during hurricane days? *Remote Sens. Environ.*, **259**, 112417, <https://doi.org/10.1016/j.rse.2021.112417>.
- Barros, A. P., and M. Arulraj, 2020: Remote sensing of orographic precipitation. *Satellite Precipitation Measurement*, V. Levizzani et al., Eds., Advances in Global Change Research, Vol. 69, Springer, 559–582, https://doi.org/10.1007/978-3-030-35798-6_6.
- Bras, R. L., and I. Rodríguez-Iturbe, 1993: Frequency-domain analysis of hydrologic signals. *Random Functions and Hydrology*, R. L. Bras and I. Rodríguez-Iturbe, Eds., Dover Publications, 155–209.
- Chambon, P., R. Roca, I. Jobard, and M. Capderou, 2013a: The sensitivity of tropical rainfall estimation from satellite to the configuration of the microwave imager constellation. *IEEE Geosci. Remote Sens. Lett.*, **10**, 996–1000, <https://doi.org/10.1109/LGRS.2012.2227668>.
- , I. Jobard, R. Roca, and N. Viltard, 2013b: An investigation of the error budget of tropical rainfall accumulation derived from merged passive microwave and infrared satellite measurements. *Quart. J. Roy. Meteor. Soc.*, **139**, 879–893, <https://doi.org/10.1002/qj.1907>.
- Chen, B. M., Z. Lin, and Y. Shamash, 2004: *Linear Systems Theory: A Structural Decomposition Approach*. Birkhäuser, 416 pp., <https://doi.org/10.1007/978-1-4612-2046-6>.
- Chen, C. T., 2012: *Linear System Theory and Design*. 4th ed. Oxford University Press, 400 pp.
- Cohen, A., I. Daubechies, and J.-C. Feauveau, 1992: Biorthogonal bases of compactly supported wavelets. *Commun. Pure Appl. Math.*, **45**, 485–560, <https://doi.org/10.1002/cpa.3160450502>.
- Cottis, R. A., A. M. Homborg, and J. M. C. Mol, 2016: The relationship between spectral and wavelet techniques for noise analysis. *Electrochim. Acta*, **202**, 277–287, <https://doi.org/10.1016/j.electacta.2015.11.148>.
- Daliakopoulos, I. N., and I. K. Tsanis, 2012: A weather radar data processing module for storm analysis. *J. Hydroinform.*, **14**, 332–344, <https://doi.org/10.2166/hydro.2011.118>.
- Derin, Y., and Coauthors, 2016: Multiregional satellite precipitation products evaluation over complex terrain. *J. Hydrometeor.*, **17**, 1817–1836, <https://doi.org/10.1175/JHM-D-15-0197.1>.
- Dooge, J., 1973: Linear theory of hydrologic systems. Tech. Bull. 1468, Agricultural Research Service, U.S. Department of Agriculture, 327 pp., <https://handle.nal.usda.gov/10113/CAT74413771>.
- Guilloteau, C., and E. Foufoula-Georgiou, 2020: Multiscale evaluation of satellite precipitation products: Effective resolution of IMERG. *Satellite Precipitation Measurement*, V. Levizzani et al., Eds., Advances in Global Change Research, Vol. 69, Springer, 533–558, https://doi.org/10.1007/978-3-030-35798-6_5.
- , R. Roca, M. Gosset, and V. Venugopal, 2018: Stochastic generation of precipitation fraction at high resolution with a multiscale constraint from satellite observations. *Quart. J. Roy. Meteor. Soc.*, **144**, 176–190, <https://doi.org/10.1002/qj.3314>.
- , E. Foufoula-Georgiou, P. Kirstetter, J. Tan, and G. J. Huffman, 2021: How well do multisatellite products capture the space–time dynamics of precipitation? Part I: Five products assessed via a wavenumber–frequency decomposition. *J. Hydrometeor.*, **22**, 2805–2823, <https://doi.org/10.1175/JHM-D-21-0075.1>.
- Hong, Y., K. L. Hsu, S. Sorooshian, and X. Gao, 2004: Precipitation Estimation from Remotely Sensed Imagery Using an Artificial Neural Network Cloud Classification System. *J. Appl. Meteor.*, **43**, 1834–1853, <https://doi.org/10.1175/JAM2173.1>.
- Huffman, G. J., R. F. Adler, B. Rudolf, U. Schneider, and P. R. Keehn, 1995: Global precipitation estimates based on a technique for combining satellite-based estimates, rain gauge analysis, and NWP model precipitation information. *J. Climate*, **8**, 1284–1295, [https://doi.org/10.1175/1520-0442\(1995\)008<1284:GPEBOA>2.0.CO;2](https://doi.org/10.1175/1520-0442(1995)008<1284:GPEBOA>2.0.CO;2).
- , and Coauthors, 2019a: NASA Global Precipitation Measurement (GPM) Integrated Multi-satellitE Retrievals for GPM (IMERG). Algorithm Theoretical Basis Doc., version 06, 34 pp., https://gpm.nasa.gov/sites/default/files/2019-05/IMERG_ATBD_V06.pdf.
- , E. F. Stocker, D. T. Bolvin, E. J. Nelkin, and J. Tan, 2019b: GPM IMERG Final Precipitation L3 Half Hourly 0.1 degree × 0.1 degree V06. Goddard Earth Sciences Data and Information Services Center (GES DISC), accessed 2 February 2021, <https://doi.org/10.5067/GPM/IMERG/3B-HH/06>.
- , —, —, —, and —, 2019c: GPM IMERG Early Precipitation L3 Half Hourly 0.1 degree × 0.1 degree V06. Goddard Earth Sciences Data and Information Services Center (GES DISC), accessed 2 February 2021, <https://doi.org/10.5067/GPM/IMERG/3B-HH-E/06>.
- Jiménez-Martínez, J., L. Longuevergne, T. Le Borgne, P. Davy, A. Russian, and O. Bour, 2013: Temporal and spatial scaling of hydraulic response to recharge in fractured aquifers: Insights

- from a frequency domain analysis. *Water Resour. Res.*, **49**, 3007–3023, <https://doi.org/10.1002/wrcr.20260>.
- Joyce, R. J., and P. Xie, 2011: Kalman filter–based CMORPH. *J. Hydrometeorol.*, **12**, 1547–1563, <https://doi.org/10.1175/JHM-D-11-022.1>.
- Jukić, D., and V. Denić-Jukić, 2004: A frequency domain approach to groundwater recharge estimation in karst. *J. Hydrol.*, **289**, 95–110, <https://doi.org/10.1016/j.jhydrol.2003.11.005>.
- Keesman, K. J., 2011: *System Identification: An Introduction*. Springer, 323 pp., <https://doi.org/10.1007/978-0-85729-522-4>.
- Kidd, C., G. Huffman, V. Maggioni, P. Chambon, and R. Oki, 2021: The global satellite precipitation constellation: Current status and future requirements. *Bull. Amer. Meteor. Soc.*, **102**, E1844–E1861, <https://doi.org/10.1175/BAMS-D-20-0299.1>.
- Kirstetter, P.-E., and Coauthors, 2012: Toward a framework for systematic error modeling of spaceborne precipitation radar with NOAA/NSSL ground radar–based National Mosaic QPE. *J. Hydrometeorol.*, **13**, 1285–1300, <https://doi.org/10.1175/JHM-D-11-0139.1>.
- , N. Viltard, and M. Gosset, 2013: An error model for instantaneous satellite rainfall estimates: evaluation of BRAIN-TMI over West Africa. *Quart. J. Roy. Meteor. Soc.*, **139**, 894–911, <https://doi.org/10.1002/qj.1964>.
- , W. A. Petersen, and J. J. Gourley, 2018: GPM Ground Validation Multi-Radar/Multi-Sensor (MRMS) Precipitation Reanalysis for Satellite Validation Product. NASA EOSDIS Global Hydrology Resource Center, accessed 27 January 2021, <https://doi.org/10.5067/GPMGV/MRMS/DATA101>.
- Kumar, P., and E. Foufoula-Georgiou, 1997: Wavelet analysis for geophysical applications. *Rev. Geophys.*, **35**, 385–412, <https://doi.org/10.1029/97RG00427>.
- Li, C., G. Tang, and Y. Hong, 2018: Cross-evaluation of ground-based, multi-satellite and reanalysis precipitation products: Applicability of the triple collocation method across mainland China. *J. Hydrol.*, **562**, 71–83, <https://doi.org/10.1016/j.jhydrol.2018.04.039>.
- Lu, X., G. Tang, X. Liu, X. Wang, Y. Liu, and M. Wei, 2021: The potential and uncertainty of triple collocation in assessing satellite precipitation products in Central Asia. *Atmos. Res.*, **252**, 105452, <https://doi.org/10.1016/j.atmosres.2021.105452>.
- Maggioni, V., M. R. Sapiano, R. F. Adler, Y. Tian, and G. J. Huffman, 2014: An error model for uncertainty quantification in high-time-resolution precipitation products. *J. Hydrometeorol.*, **15**, 1274–1292, <https://doi.org/10.1175/JHM-D-13-0112.1>.
- , M. R. P. Sapiano, and R. F. Adler, 2016: Estimating uncertainties in high-resolution satellite precipitation products: Systematic or random error? *J. Hydrometeorol.*, **17**, 1119–1129, <https://doi.org/10.1175/JHM-D-15-0094.1>.
- Mastrantonas, N., B. Bhattacharya, Y. Shibuo, M. Rasmy, G. Espinoza-Dávalos, and D. Solomatine, 2019: Evaluating the benefits of merging near-real-time satellite precipitation products: A case study in the Kinu basin region, Japan. *J. Hydrometeorol.*, **20**, 1213–1233, <https://doi.org/10.1175/JHM-D-18-0190.1>.
- Petersen, W. A., P.-E. Kirstetter, J. Wang, D. B. Wolff, and A. Tokay, 2020: The GPM ground validation program. *Satellite Precipitation Measurement*, V. Levizzani et al., Eds., Advances in Global Change Research, Vol. 69, Springer, 471–502, https://doi.org/10.1007/978-3-030-35798-6_2.
- Pradhan, R. K., and Coauthors, 2022: Review of GPM IMERG performance: A global perspective. *Remote Sens. Environ.*, **268**, 112754, <https://doi.org/10.1016/j.rse.2021.112754>.
- Rajagopal, M., E. Zipser, G. Huffman, J. Russell, and J. Tan, 2021: Comparisons of IMERG version 06 precipitation at and between passive microwave overpasses in the tropics. *J. Hydrometeorol.*, **22**, 2117–2130, <https://doi.org/10.1175/JHM-D-20-0226.1>.
- Roca, R., and Coauthors, 2021: The joint IPWG/GEWEX precipitation assessment. WCRP Publ. 2/2021, 125 pp., <https://doi.org/10.13021/gewex.precip>.
- Rossa, A., P. Nurmi, and E. Ebert, 2008: Overview of methods for the verification of quantitative precipitation forecasts. *Precipitation: Advances in Measurement, Estimation and Prediction*, S. Michaelides, Ed., Springer, 419–452, https://doi.org/10.1007/978-3-540-77655-0_16.
- Schuite, J., N. Flipo, N. Massei, A. Rivière, and F. Baratelli, 2019: Improving the spectral analysis of hydrological signals to efficiently constrain watershed properties. *Water Resour. Res.*, **55**, 4043–4065, <https://doi.org/10.1029/2018WR024579>.
- Subramani, P., R. Sahu, and S. Verma, 2006: Feature selection using Haar wavelet power spectrum. *BMC Bioinf.*, **7**, 432, <https://doi.org/10.1186/1471-2105-7-432>.
- Swisher, G. M., 1976: *Introduction to Linear Systems Analysis*. Matrix Publishers, 724 pp.
- Tang, G., 2020: Characterization of the systematic and random errors in satellite precipitation using the multiplicative error model. *IEEE Trans. Geosci. Remote Sens.*, **59**, 5407–5416, <https://doi.org/10.1109/TGRS.2020.3028525>.
- Tang, S., R. Li, and J. He, 2021: Modeling and evaluating systematic and random errors in multiscale GPM IMERG summer precipitation estimates over the Sichuan basin. *IEEE J. Sel. Top. Appl. Earth Obs. Remote Sens.*, **14**, 4709–4719, <https://doi.org/10.1109/JSTARS.2021.3076197>.
- Tian, Y., G. J. Huffman, R. F. Adler, L. Tang, M. Sapiano, V. Maggioni, and H. Wu, 2013: Modeling errors in daily precipitation measurements: Additive or multiplicative? *Geophys. Res. Lett.*, **40**, 2060–2065, <https://doi.org/10.1002/grl.50320>.
- Turk, F. J., B.-J. Sohn, H.-J. Oh, E. E. Ebert, V. Levizzani, and E. A. Smith, 2009: Validating a rapid-update satellite precipitation analysis across telescoping space and time scales. *Meteor. Atmos. Phys.*, **105**, 99–108, <https://doi.org/10.1007/s00703-009-0037-4>.
- Ushio, T., and Coauthors, 2009: A Kalman filter approach to the Global Satellite Mapping of Precipitation (GSMaP) from combined passive microwave and infrared radiometric data. *J. Meteor. Soc. Japan*, **87A**, 137–151, <https://doi.org/10.2151/jmsj.87A.137>.
- Utsumi, N., H. Kim, F. J. Turk, and Z. S. Haddad, 2019: Improving satellite-based subhourly surface rain estimates using vertical rain profile information. *J. Hydrometeorol.*, **20**, 1015–1026, <https://doi.org/10.1175/JHM-D-18-0225.1>.
- Vaseghi, S. V., 2008: Wiener filters. *Advanced Digital Signal Processing and Noise Reduction*, S. V. Vaseghi, Ed., John Wiley and Sons, 178–204.
- Welch, P., 1967: The use of fast Fourier transform for the estimation of power spectra: A method based on time averaging over short, modified periodograms. *IEEE Trans. Audio Electroacoust.*, **15**, 70–73, <https://doi.org/10.1109/TAU.1967.1161901>.
- Whitcher, B., 2020: Package ‘waveslim.’ R package, version 1.8.3, 81 pp., <https://cran.r-project.org/web/packages/waveslim/waveslim.pdf>.
- Wiener, N., 1949: *Extrapolation, Interpolation, and Smoothing of Stationary Time Series*. MIT Press, 163 pp.
- Wright, D. B., D. B. Kirschbaum, and S. Yatheendradas, 2017: Satellite precipitation characterization, error modeling, and error correction using censored shifted gamma distributions.

- J. Hydrometeor.*, **18**, 2801–2815, <https://doi.org/10.1175/JHM-D-17-0060.1>.
- Xie, P. R. Joyce, S. Wu, S.-H. Yoo, Y. Yarosh, F. Sun, and R. Lin, 2019: NOAA Climate Data Record (CDR) of CPC Morphing Technique (CMORPH) High Resolution Global Precipitation Estimates, version 1. NOAA National Centers for Environmental Information, accessed 2 February 2021, <https://doi.org/10.25921/w9va-q159>.
- You, Y., V. Petkovic, J. Tan, R. Kroodsma, W. Berg, C. Kidd, and C. Peters-Lidard, 2020: Evaluation of V05 precipitation estimates from GPM constellation radiometers using KuPR as the reference. *J. Hydrometeor.*, **21**, 705–728, <https://doi.org/10.1175/JHM-D-19-0144.1>.
- Zhang, Z., 2018: Multivariate wavelets. *Multivariate Time Series Analysis in Climate and Environmental Research*, Z. Zhang, Ed., Springer, 97–148, https://doi.org/10.1007/978-3-319-67340-0_3.